CHAPTER 12

On Transitions in Granular Packings Exposed to Compression

KIANOOSH TAGHIZADEH, a,b RITUPARNA BASAK AND LOU KONDIC*c

^a Multi-Scale Mechanics, TFE-ET, MESA+, University of Twente, 7500AE Enschede, The Netherlands; ^b Institute of Applied Mechanics (CE), University of Stuttgart, 70569 Stuttgart, Germany; ^c Department of Mathematical Sciences, New Jersey Institute of Technology, University Heights, Newark, NJ 07102, USA

*Email: kondic@njit.edu

Introduction 12.1

Granular materials, although ubiquitous in nature and widely used in engineering and construction, remain relatively poorly understood. They may behave like solids, liquids, or gases, though typically exhibiting a variety of unexpected behaviors. Complex systems, such as dense granular media, exhibit intriguing phenomena even in simple cases like monodisperse disk packings, such as arching or jamming. The confinement imposed by the sample boundaries necessitates a balance of inter-particle contact forces to maintain mechanical equilibrium. The formal description of the structural complexity of such systems has only been achieved in recent times. The preponderance of problems yet to be solved has sparked a renewed interest in granular materials, in different communities.

Theoretical and Computational Chemistry Series No. 27 Packing Problems in Soft Matter Physics: Fundamentals and Applications Edited by Ho-Kei Chan, Stefan Hutzler, Adil Mughal, Corey S. O'Hern, Yujie Wang and Denis Weaire

[©] The Royal Society of Chemistry 2025 Published by the Royal Society of Chemistry, www.rsc.org

Granular materials behave differently from usual solids or fluids and show peculiar mechanical properties such as dilatancy or ratcheting.^{1,2} One interesting characteristic of these materials is their sensitivity to external stress. In densely packed systems, for instance, the external pressure can cause the system to transition between rigid and floppy states, the so-called jamming transition typical of many amorphous materials. Since the system becomes rigid and can carry loads, jamming defines the threshold at which the elastic stiffness of the assembly assumes finite values.^{3,4}

The discrete element method (DEM)⁵⁻⁹ has become increasingly popular in recent decades as a computational tool for modeling granular systems in both academia and industry. With advancements in particle simulation methods and increasing computer power, DEM has seen widespread use for understanding the behavior of granules qualitatively and quantitatively. It allows us to explore the physics of discrete particulate systems, which traditional continuum solid/fluid mechanics cannot explain.¹⁰

In micromechanical and numerical studies, the elastic response of a granular packing is associated with the deformations of a fixed contact network, and should therefore correspond to the "true elastic" behavior observed in the laboratory for very small strain intervals. When particle network rearrangement occurs, the sample is considered to have undergone a plastic response that is irreversible. Indeed, except in very special situations in which the effects of friction are suppressed, and geometric restructuring is reversible, the irreversible changes associated with network alterations or rearrangements preclude continuous modeling, 12–15 motivating DEM simulations further.

During compression of jammed granular assemblies, if the applied rate is kept small enough, the assemblies change from one equilibrium state to another. Before events, the assembly is considered in mechanical equilibrium with an elastic (reversible) response. When the sample reconfigures itself (a so-called "event" took place) to reach a new mechanical equilibrium, it will no longer remain in its initial elastic regime but a new elastic regime is established according to the new equilibrium configuration. Thus, the sample experiences an initial elastic response, an event that is the source of the plastic response, and a new elastic response according to the new configuration.

The current study doesn't aim to investigate the plasticity (*i.e.*, irreversible) behavior of granular assemblies; rather, we focus on transient regimes spanning from elastic to plastic behavior. Earlier studies have shown that in a steady-state shear flow, continuous shear induces constant contact breaking, rendering the transient regime largely overlooked. The advantage of employing isotropic compression lies in capturing elastic behavior during compression. Here, particles remain stationary, undergoing local rearrangements (so-called events) swiftly returning the sample to a new elastic state. It is crucial to note that our study seeks to illustrate the impact of these local rearrangements (transients) on the global assembly. By quantifying the energy ratio as a macroscopic parameter, we aim to show how these events influence the overall system.

The research outlined in this chapter specifically targets dry polydisperse frictional granular particles in a jammed state. The main objective is to investigate how different input parameters (at the particle scale) impact the contact networks (a macroscopic property) of these particle packings. By understanding the influence of microscopic parameters on the macroscopic properties of the packings, ^{16–18} we aim to advance the development of constitutive models that can accurately predict material behavior at a larger scale.

We consider a very simple setup: a cubic granular domain exposed to temporally varying externally applied compression and relaxation. First, we discuss the overall features of the compression, and then we focus on the influence of various simulation parameters on the manner in which the considered granular system responds to externally applied forcing. Even in simple geometry and under controlled forcing, granular packings respond in a nontrivial manner, which is strongly imposed by the problem parameters, in particular friction. In this chapter, we discuss the main features of the results only, and in particular, we focus only on the insight that can be obtained by considering the system's kinetic and potential energies. The interested reader may find much more in-depth discussion in our recent works, 19,20 where in addition to consideration of the energies, we also analyze statics and dynamics of the force networks determining the interactions between the particles. 21,22

The rest of this chapter is organized as follows: in Section 12.2, we introduce the Discrete Element Method; then, we describe the sample preparation and input parameters in Section 12.2.2. Section 12.3 explores the effect of simulation input parameters on the energy response of frictional packings. Finally, our conclusions are presented in Section 12.4.

12.2 Numerical Simulation – Discrete Element Method

The Discrete Element Method (DEM) is a simple algorithm used to solve equations of motion, both translation and rotational, for multiple interacting particles. The algorithm solves:

$$m_i \vec{a}_i = \vec{f}_i + \gamma_b \vec{v}_i + m_i \vec{g}$$

$$I_i \vec{\omega}_i = \vec{\tau}_i + \gamma_{br} r_i^2 \vec{\omega}_i$$
(12.1)

where m_i is the mass of the *i*-th particle, r_i its radius, I_i its (spherical) moment of inertia, with particle position \vec{x}_i , velocity $\vec{v}_i = \vec{x}$, acceleration $\vec{a}_i = \vec{x}$, and angular velocity $\vec{\omega}_i$.

The forces acting on the particles can be grouped into three categories: (i) volume forces due to gravity (ignored in the present work), (ii) background damping forces, with dissipation coefficients γ_b and γ_{br} , accounting for energy loss caused by viscous drag from a background medium (explained

further in the next section), and (iii) contact forces between particles: $\vec{f}_i = \sum_c \vec{f}_i^c$, as well as the torques: $\vec{\tau}_i = \sum_c \left(\vec{l}_i^c \times \vec{f}_i^c + \vec{q}_i^r + \vec{q}_i^t \right)$, where \vec{l}_i^c is the branch vector. In the present study, the torques due to rolling and torsion.

branch vector. In the present study, the torques due to rolling and torsion, \vec{q}_i^r , \vec{q}_i^t , are neglected.

12.2.1 Force Laws

The force laws used in DEM are based on the relationship between the forces and the overlap or deformation between two particles, which are decomposed into normal and tangential components $(\vec{f}_i^c = \vec{f}^n + \vec{f}^t)$. By integrating the equations of motion with a time-step Δt using the given normal and tangential forces acting on all contact points c, the positions of the particles can be obtained over time. 23,24

12.2.1.1 Normal Force Law

Normal interaction forces are computed using the normal overlap δ^n between two particles (modeled as spheres here) to determine the interaction force. Two particles interact only if they are in contact, which occurs when there is a positive overlap between them. The overlap in the normal direction is given by eqn (12.2), where $\vec{n} = (\vec{x}_i - \vec{x}_j)/|\vec{x}_i - \vec{x}_j|$ is the unit vector pointing from the centroid of particle j to particle i, and r_i are the radii of the two particles.

$$\delta^{n} = (r_{i} + r_{j}) - (\vec{x}_{i} - \vec{x}_{j}) \cdot \vec{n} > 0.$$
 (12.2)

The most basic contact model in DEM is the linear spring-dashpot viscoelastic force magnitude. ^{6,8,25-27} This model assumes that particles are nearly spherical and do not deform significantly during an interaction, and therefore requires limiting overlaps to small values compared to particle diameter, typically less 10%. Additionally, this model considers only binary, pair contacts between particles. The contact force law is given by:

$$f^{n} = f_{\text{el}}^{n} + f_{\text{visc}}^{n} = k_{n} \delta^{n} + \gamma_{n} \dot{\delta}^{n}, \qquad (12.3)$$

where f^n is the contact force magnitude, k_n is the spring constant, and γ_n is the damping coefficient. The damping coefficient causes dissipation proportional to the relative normal velocity between the two particles, which is denoted by $\dot{\delta}^n$ and can be expressed as $v_{\rm rel}^n = -(\vec{v}_i - \vec{v}_j) \cdot \vec{n}$.

12.2.1.2 Tangential Force Law

There is a wide range of force models for tangential forces resulting from oblique particle impacts. ^{27–30} In this study, we use a model based on the theory of Mindlin, ³¹ as described in ref. 32 to account for tangential forces.

When two surfaces in contact experience increasing tangential displacement, denoted as δ^t , relative slip begins at the perimeter and propagates inward over an annular region of the contact surface. An approach based on the constant normal force solution of Mindlin was proposed already in ref. 33. Analogously to the normal force, the tangential force involves a linear (tangential) spring with stiffness k_t and a viscous damping with γ_t , similar to the model used in ref. 32, 34, and 35. The linear viscoelastic tangential test force magnitude:

$$\vec{f}^t = \vec{f}_{el}^t + \vec{f}_{visc}^t = k_t \vec{\delta}^t + \gamma_t \vec{\delta}^t$$
 (12.4)

involves damping proportional to the tangential velocity $\vec{v}^t = \vec{\delta}^t$.

To obtain the elastic tangential displacement, δ^t , the relative tangential velocity vector is integrated during elastic deformations, as explained in ref. 32, 36, and 37. The tangential force described in eqn (12.4) is subject to Coulomb's criterion for particle contact friction. When the tangential force is greater than or equal to $\mu_d f^n$, where μ_d is the dynamic friction coefficient, dynamic friction occurs. On the other hand, when the tangential force is less than or equal to $\mu_s f^n$, where μ_s is the static friction coefficient, elastic static friction is active. Further details are provided in ref. 32; in the present work, for simplicity, we assume that $\mu_s = \mu_d = \mu$.

12.2.1.3 Background Damping

To mitigate dynamic effects and expedite relaxation times, an artificial damping force and torque, denoted as \vec{f}^b and \vec{q}^{br} , are introduced. They are designed to mimic the damping characteristics observed in background media, such as fluids. Unlike traditional damping forces acting on contacts, $\vec{f}^b_i = -\gamma_b \vec{v}_i$ and $\vec{q}^{br}_i = -\gamma_{br} r_i^2 \vec{\omega}_i^2$ directly affect particles, and their magnitude is proportional to their velocity and angular velocity. By incorporating the artificial damping force and torque, the system can effectively mimic the damping behavior experienced in the presence of a surrounding medium, contributing to improved simulation accuracy and more realistic dynamic responses. Therefore, additional damping with the background can be introduced, so that the total force and torque on particle i become:

$$\vec{f}_{i} = \sum_{c} \vec{f}_{i}^{c} + \vec{f}_{i}^{b}, \tag{12.5}$$

$$\vec{\tau}_i = \sum_c \left(\vec{l}_i^c \times \vec{f}_i^c \right) + \vec{q}_i^{\text{br}}. \tag{12.6}$$

12.2.2 Sample Preparation

To generate the samples, particles are randomly created within a 3D box at a very low volume fraction, ϕ . Each particle is assigned a small velocity, resulting in their movement, collision, and randomization. To prevent

crystallization, the spheres are polydisperse, characterized by a uniform size distribution with a width ($w = r_{\text{max}}/r_{\text{min}} = 3$), where $\langle r \rangle$ represents the average radius, with r_{max} and r_{min} corresponding to the radii of the largest and smallest particles, respectively. After random generation, the packing is isotropically compressed to the target $\phi_1 = 0.5$, which is well below the jamming (the transition from fluid- to solid-like behavior in the granular matter) regime ϕ_L^{38} The system is then relaxed at ϕ_1 , and particles are allowed to dissipate their kinetic energy and reach zero pressure. Next, further isotropic compression is applied up to a volume fraction of $\phi_{\rm max} = 0.82$. ^{8,35} The compression during the sample preparation is performed using a constant isotropic strain rate $(\dot{\epsilon}_{\nu} = 10^{-7})$ applied to each particle to ensure the homogeneity of the sample. In Section 12.3.2.1, we study the effect of the applied rate on the response of assemblies for a specific compression window which is explained in the next section. We note that large deformations can lead to the formation of new contacts among particles, among other effects. Recent studies have addressed the realistic behavior of highly deformable particles through both numerical methods^{34,39,40} and experimental approaches; 41-44 in the present work we do not consider such effects and instead employ a commonly used DEM approach to simulate the compaction of "soft" elastic grains.

Table 12.1 provides the base set of parameters for DEM simulations. When any contact parameter is adjusted, the remaining parameters are selected from the values listed in this table, which also specifies the values used for non-dimensionalization, t_u , x_u , and m_u , for time, space, and mass, respectively. All the results that follow are presented using these scales, with the exception of pressure which is also scaled by the (dimensionless) value of

Table 12.1 The microscopic contact model parameters serve as the fundamental parameters for the simulations unless otherwise specified. The first and second columns define the meaning of the symbols. The third column contains (dimensionless) values used in DEM, and the fourth column contains the (dimensional) physical quantities in SI units.

Property	Symbol	Dimensionless	Dimensional [SI unit]
Time unit	t_u	1	10^{-4} s
Length unit	x_u	1	10^{-3} m
Mass unit	m_u	1	10^{-9} kg
Average particle radius	$\langle r \rangle$	1	10^{-3} m
Polydispersity	$r_{\rm max}/r_{\rm min}$	3	
Number of particles	N	4096	
Particle density	ρ	2000	2000 kg m^{-3}
Simulation time step	$\Delta t_{ ext{MD}}$	0.0037	$3.7 \ 10^{-9} \ s$
Normal stiffness	k_n	10^{5}	$10^4 \mathrm{kg s^{-2}}$
Tangential stiffness	k_t/k_n	0.2	_
Coefficient of friction	μ	0.0001, 0.1, 1	
Normal viscosity	γ_n	1000	$10^{-2} \text{ kg s}^{-1}$
Tangential viscosity	γ_t/γ_n	0.2	· ·
Background viscosity	γ_b/γ_n	0.1	
Background torque viscosity	$\gamma_{\mathrm{br}}/\gamma_{n}$	0.02	

 k_n/d , where $d = 2\langle r \rangle$. More precisely, the dimensional pressure p_D (in the SI units) can be obtained from the non-dimensional one reported in the results (p) as $p_D = (m_u/(x_u t_u^2))(k_n/d)p$.

Granular materials exhibit a captivating dual nature, displaying characteristics of both solids and fluids. Understanding their behavior involves categorizing granular flows into three distinct regimes. First, at low deformation rates, granular particles remain in contact, engaging in prolonged interactions with their neighbors, defining the quasi-static regime. Second, as the deformation rate increases, granular materials transition into a dense flow state, resembling the behavior of a liquid. In this regime, particles experience frequent multi-contact interactions, and the transition between quasi-static and dense flow is marked by the jamming point, where flow ceases. Third, at extremely high velocities, granular media exhibit gas-like behavior, characterized by brief binary interactions between particles due to the rapid nature of their contacts. The transition between these regimes can be identified using a dimensionless parameter so-called volumetric inertial number, $(I_v = \dot{\varepsilon}_v d\sqrt{\rho/p})$. The inertial number reflects the ratio of the microscopic inertial time scale $(d\sqrt{\rho/p})$, also known as the particle relaxation time) to the macroscopic time scale associated with the applied rate $(\dot{\varepsilon}_{v})$. When I_{ν} is less than 0.001, the flow approaches the quasi-static limit, characterized by a dense network of enduring contacts. 49,50 In the range of $(0.001 < I_{\nu} < 0.01)$, the transition from quasi-static to inertial flow occurs. Within the interval of $(0.01 < I_v < 1)$, the flow enters an intermediate fluidlike regime where dynamic inertial effects play a crucial role. To ensure the simulations are slow enough to be in the quasi-static and rate-independent regime, the inertial number for the slow rate $(\dot{\epsilon}_{\nu} \approx 10^{-7})$ at small $p \ge 10^{-2}$, is $I_{\nu} \approx 10^{-5}$, confirming that the simulations are in the quasi-static, rateindependent regime.

12.3 Results

12.3.1 Big Picture: Full Compression Branch

The simulations are conducted using particles characterized by a few different values of the contact friction coefficients, $\mu=0.0001,\,0.1,\,$ and 1, all starting from the same initial configuration at ϕ_0 , which originates from $\mu=0.^{19}$ Figure 12.1(a) displays the dimensionless pressure obtained from simulations of isotropic compression. We observe a rise in pressure as the samples are compressed. Moreover, for a given value of ϕ , the pressure increases with μ . This is not a surprise, since earlier studies, see e.g. ref. 51 and 52, have shown that jamming is significantly impacted by friction. As a result, samples with the same value of ϕ exhibit considerable variations in both microscopic properties, such as coordination number (the average number of contacts of a particle), and macroscopic features, such as pressure. Consequently, comparing packings characterized by different values of μ at the same value of ϕ may be confusing. Instead, we

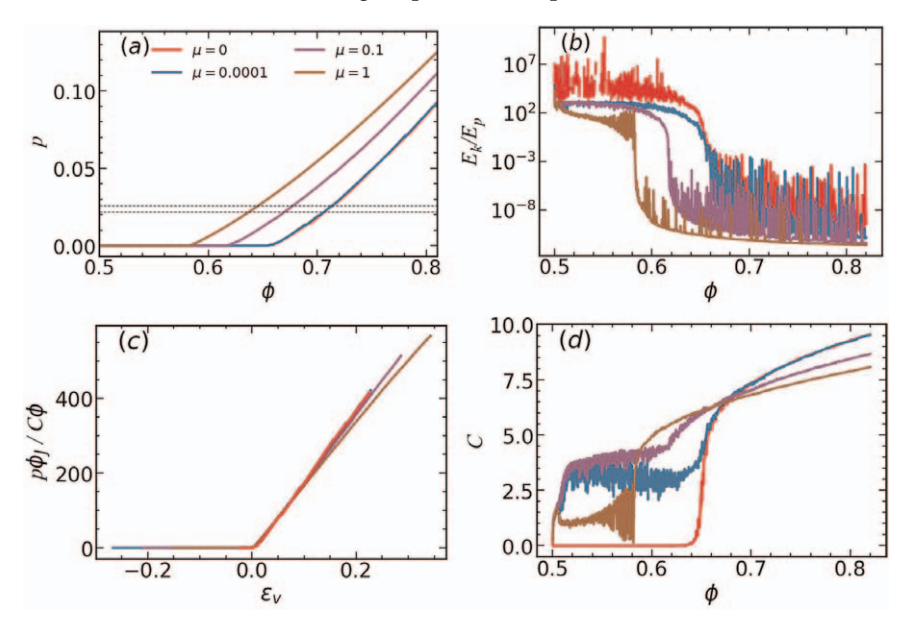


Figure 12.1 (a) Pressure p, (b) energy ratio (E_k/E_p) , plotted against volume fraction ϕ for selected values of friction coefficients μ during sample compression. Note that the results for $\mu=0$ and $\mu=0.0001$ are essentially overlapping; (c) scaled pressure $(p\phi_J/C\phi)$ plotted as a function of volumetric strain; and (d) coordination number C plotted against volume fraction ϕ .

proceed by comparing the results for packings characterized by a specified pressure range. The range considered in this work is shown by the dashed lines in Figure 12.1(a). In precise terms, after loading the samples, a configuration at a typical pressure of $p_z = 0.022$ is selected; this value is depicted in Figure 12.1 by the lower dotted line. Then, these configurations are further compressed from p_z to $p_z + 0.004$ (shown by the upper dotted line in Figure 12.1) at a smaller isotropic strain rate of $\dot{\varepsilon}_v = 10^{-8}$.

Based on Figure 12.1(a) one may conclude that the evolution of the compressed packings is smooth. However, consideration of the ratio of kinetic and potential energy of the packings, Figure 12.1(b), shows that this is not the case. 53,54 Here, for simplicity, the kinetic energy, E_k , includes only the contribution from the translation degrees of freedom; the kinetic energy associated with rotations is typically much smaller and shows similar features as the translation kinetic energy. Furthermore, to visualize more clearly the most interesting contributions to kinetic energy, we have subtracted the affine part, which has to do with uniform compression (see ref. 19 and 20 for more details). The potential energy consists of two components: the normal and the tangential contributions. Figure 12.1(b) shows that an increase in μ causes a decrease in the kinetic energy for a given value of ϕ . This is expected

since larger friction leads to stronger dissipation and larger tangential components of force, therefore decreasing the mobility of particles and the kinetic energy. As already noted above, the ratio of the energies shows that the evolution of the packings is far from smooth, but instead, it involves a large number of "peaks" which, as we will discuss in more detail in what follows, correspond to transitions, that are due to rearrangements of the considered packings. We note that it is indeed E_k that changes during transitions; E_p , similarly to the pressure, is essentially constant on the time-scale of the transitions.

Previous studies have presented^{51,55} an analytical expression for the dimensionless pressure in assemblies of polydisperse particles, which is applicable to a wide range of volume fractions above the jamming regime

$$p = \lambda \frac{\phi C}{\phi_I} (-\varepsilon_v) \Big[1 - \gamma_p (-\varepsilon_v) \Big]. \tag{12.7}$$

Here, C represents the coordination number, ϕ_J signifies the jamming fraction at which the pressure becomes zero during unloading, ε_ν denotes the compressive volumetric strain applied to the particle packing ($\varepsilon_\nu = \ln(\phi_J/\phi)$), and λ and γ_p are fitting parameters. The equation relies on the jamming fraction, ϕ_J , which cannot be determined from the fits and must be independently calculated. During isotropic compression, ϕ_J represents the volume fraction at which the pressure is larger than zero, signifying the gain of mechanical stability in the system. We define ϕ_J using an energy criterion, stating that it is the first point on the volume fraction axis where the energy ratio falls below 10^{-5} . It is worth mentioning that there is no precise definition of ϕ_J , and similar criteria have been considered by other researchers δ_J , δ_J ,

Figure 12.1(c) shows the scaled dimensionless pressure, obtained by dividing the inverse contact density by the jamming fraction. Unlike previous studies on frictionless polydisperse systems, ⁵¹ the data points do not perfectly collapse on a single line. However, a linear relationship with strain is evident from the figure. This indicates that the impact of particle friction on pressure cannot be solely evaluated based on contact density and critical volume fraction. In addition, Figure 12.1(d) shows the coordination number plotted against the volume fraction. ^{60–62} As particle friction increases, C decreases, approaching the value of four. Table 12.2 summarizes the DEM outcomes for packings at jamming and at p_z .

Figure 12.1 shows that the friction coefficient plays a vital role in determining the response of granular packings. However, friction is not the only controlling parameter. In subsequent sections, we discuss the impact of both externally applied strain rate and other parameters describing particle interactions with the purpose of understanding in more detail the evolution of compressed granular packings, in particular regarding the rearrangements leading to transitions.

Table 12.2 Packings at the pressure p_z = 0.022 for samples with friction coefficients μ = 0, 0.0001, 0.1, and 1. Here, ϕ_J represents the jamming volume fraction of packings prepared using different μ values, C_J is the coordination number at the jamming volume fraction, and ϕ_z , E_k/E_p represents the volume fraction and the ratio of kinetic to potential energy corresponding to the selected pressure p_z . Note that the difference between ϕ_z and ϕ_J is approximately 0.056 \pm 0.002 for all values of μ .

μ	ϕ_J	C_J	ϕ_Z	E_k/E_p
0	0.654	5.95	0.707	77×10^{-10}
10^{-4}	0.653	5.91	0.706	20×10^{-10}
0.1	0.616	5.18	0.672	1.6×10^{-10}
1	0.582	4.63	0.638	0.3×10^{-10}

12.3.2 Transitions

In what follows, we focus on the pressure range bounded by the dotted lines in Figure 12.1 and discuss the influence of a few control variables on the evolution of the samples. Understanding their influence helps us to understand the nature of the evolution of jammed granular systems exposed to compression. For brevity and simplicity, we focus on frictional systems only; an in-depth study of frictionless systems can be found in ref .19

Figure 12.2(a) depicts the kinetic to potential energy ratio (0.3×10^{-10}) in the chosen pressure window, for systems with three different values of E_k/E_p and 1. The evolution is not smooth:^{53,54} it proceeds along the base-line, interrupted by discrete transient "events". As $\mu = 0.0001$, 0.1, increases, both the base-line value and the number of events decrease (in particular, for μ , there is only one event in this pressure window; further inspection finds a very limited number of events on the whole loading branch). While the small friction data are very noisy around their base-lines, they are almost perfectly flat for large $\mu = 1$.

Figure 12.2(b) illustrates the coordination number, C, for the same samples as in Figure 12.2(a). It is clear that similarly to the energy ratio plot, the evolution depicted is interrupted by the events. Also, increasing μ shows a smaller number of transients in the coordination plot. This reduction in events with increasing μ can be explained by the increase in the magnitude of tangential forces, which limit the particles' motion. Although samples with higher friction exhibit lower coordination numbers, the enhanced resistance to movement due to tangential forces makes particle rearrangement, which leads to events, more challenging.

To support the hypothesis that the temporary changes in the system correspond to a restructuring of the packing, Figure 12.2(c) displays gained and lost contacts obtained by comparing consecutive snapshots. This comparison offers insights into how the microstructure evolves during the loading process. In Figure 12.2(c), the red and blue curves represent gained

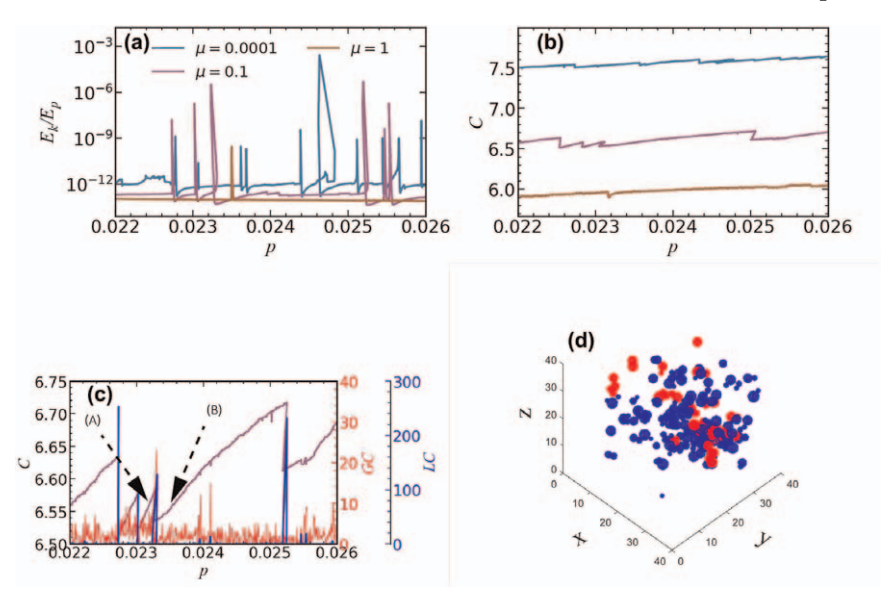


Figure 12.2 (a) Energy ratio, E_k/E_p , and (b) coordination number, C, plotted against pressure, from $p_z = 0.022$ up to 0.026 for $\mu = 0.0001$, 0.1, and 1 for samples prepared with strain rate $\dot{\varepsilon}_v = 10^{-8}$ for different μ . (c) Gained (GC, red data) and lost contacts (LC, blue data) of the sample with friction $\mu = 0.1$, on top of the coordination number (violet), plotted against pressure, for the same window as in (b). (d) Red and blue particles depict the creation of new contacts and the loss of contacts when two frames are considered: before (A) and after (B) of one large event (frames A, B marked in (c)); around 25 contacts are gained, and around 150 are lost.

and lost contacts, respectively. Contacts are gradually formed during smooth loading phases, but there are sudden and significant losses of many contacts during specific events. Prior to events, the assembly is regarded as being in a state of mechanical equilibrium with an elastic (reversible) response, as indicated by the A-point in Figure 12.2(c). However, when the sample undergoes reconfiguration during events to attain a new mechanical equilibrium (refer to B-point in Figure 12.2(c)), it no longer maintains its original elastic regime. Instead, a new elastic regime is established based on the updated equilibrium configuration. As can be seen from Figure 12.2, these transitions (elastic-plastic-elastic) are happening in a very short time since the packings are well above jammings. In Figure 12.2(d), a visual contrast of the microstructure is presented before and after an event, denoted by points A and B in Figure 12.2(c). This comparison highlights particles that have established new contacts, depicted in red, and particles that have lost contacts, depicted in blue. This analysis confirms the presence of substantial, irreversible events. These events indicate that the system shifts from one stable state to another, establishing a new equilibrium. These observations align with previous studies exploring similar phenomena. 14,63-65

12.3.2.1 Strain Rate Variation

Figure 12.3 shows the ratio of kinetic to potential energy (E_k/E_p) of systems with varying strain rate, $\dot{\varepsilon}_{\nu}$, for three considered values of μ . We see that the kinetic to potential energy ratio does not change continuously but rather follows an intermittent pattern with distinct transitions. These transitions are identified by sudden and significant changes in the energy ratio and are typically accompanied by slight decreases in pressure (not shown for brevity).

Figure 12.3 includes a significant amount of information. Focusing first on the role of μ , we observe that the number of transitions (shown by sudden jumps of E_k/E_p ratio) decreases significantly, suggesting that friction makes the evolution smoother and removes dramatic changes in the energy ratio. The transitions themselves typically consist of a sudden increase of E_k/E_p , followed by relaxation to a value that may be below the baseline of the E_k/E_p ratio. These undershoots, if present, then relax to the base-line; the transitions shown in Figure 12.3(a) and (b) for $\dot{\epsilon}_{\nu}=10^{-9}$ illustrate this pattern most clearly.

Switching our attention now to the role of the strain rate, the immediate first and most obvious observation is the scaling of E_k/E_p ratio with $\dot{\varepsilon}_{\nu}^2$: note that this observation is not necessarily obvious, since we have removed the affine contribution to the kinetic energy. The influence of the strain rate is, however, more subtle than this: focusing for clarity on the results shown in Figure 12.3(b), we observe that the transitions themselves are modified by the strain rate value, with two obvious differences between the results for different strain rates. First, the decay of energy from the peaks is faster (when plotted against pressure) for smaller $\dot{\varepsilon}_{\nu}$; however, we need to remember that the pressure changes are slower as a function of time for smaller $\dot{\varepsilon}_{\nu}$; additional inspection of the results shows that the energy decay in time is similar for all values of $\dot{\varepsilon}_{\nu}$. Second, the undershoots below the baseline occur only if the system is compressed slowly enough since the particles have enough time to relax to their most stable configuration before the system is compressed further; therefore, for the results shown in Figure 12.3(b), the undershoots are visible for $\dot{\epsilon}_{\nu} = 10^{-8}$ and 10^{-9} only (and similarly for Figure 12.3(a)). Undershoots are not observed for the $\mu = 1$ samples since the tangential components of the interparticle forces are large enough to dissipate energy quickly after an event.

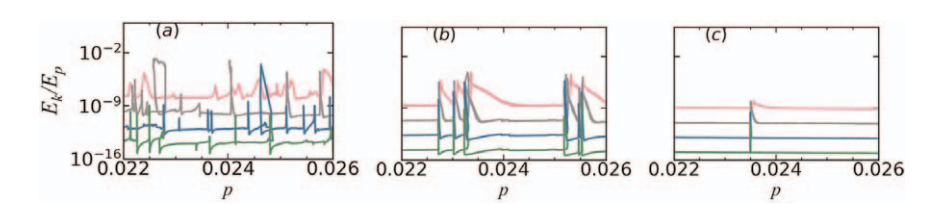


Figure 12.3 Energy ratio E_k/E_p for (a) $\mu=0.0001$, (b) $\mu=0.1$, and (c) $\mu=1$ for different strain rates. The data for different strain rates are presented in the following manner: $\dot{\varepsilon}_{\nu}=10^{-6}$ (red), $\dot{\varepsilon}_{\nu}=10^{-7}$ (grey), $\dot{\varepsilon}_{\nu}=10^{-8}$ (blue), $\dot{\varepsilon}_{\nu}=10^{-9}$ (green).

We also note that when friction is small (μ =0.0001), the number of rearrangements (transitions) and their pressure are affected by changes in the strain rate. This occurs since the tangential forces are much smaller than the normal forces; therefore, the particles rearrange more often before reaching a new equilibrium state; lower strain rates result in smoother behavior, though. On the contrary, for μ =0.1 and 1, the number of transitions is independent of the strain rate. However, the magnitude of the energy ratio during these transitions is influenced by the applied strain rate; larger strain rates lead to a smaller peak magnitude relative to the baseline.

12.3.2.2 Tangential Stiffness k_t

The next adjustable simulation parameter is the particles' tangential stiffness, which becomes active when friction is present. Since granular packings manifest different properties as their frictional properties are modified, we repeat the preparation step for the results presented here. The parameters used are the ones specified in Table 12.1, except for k_t , which is varied as $k_t/k_n = 0.001, 0.01, 0.1, 0.2, 0.5, 0.8$ (k_n is kept fixed).

Figure 12.4 shows the energy ratio, E_k/E_p , for the considered pressure window for the listed values of k_t/k_n and three values of μ . By comparing the results obtained for different values of k_t and fixed μ , we observe that for larger values of μ , increasing k_t decreases the base-line of the energy ratio. This finding can be explained by the fact that an increase in tangential stiffness leads to larger tangential forces, resulting in fewer particle rearrangements and a decrease in the kinetic energy. This effect becomes less visible for smaller values of μ (e.g. for μ = 0.0001) since for such values of μ the tangential forces lose their relevance.

As mentioned earlier, friction between particles plays a key role in configuration rearrangements (transitions), with an increase in friction leading to fewer transitions/rearrangements during compression. When comparing the results for different values of k_t for a constant μ , we find that k_t plays a similar role to friction; an increase in k_t results in a reduced number of transitions as particles become more constrained in their movement.

Lastly, we examine the effect of k_t on the undershoots. It has been shown previously in the section that the magnitude of the undershoots is

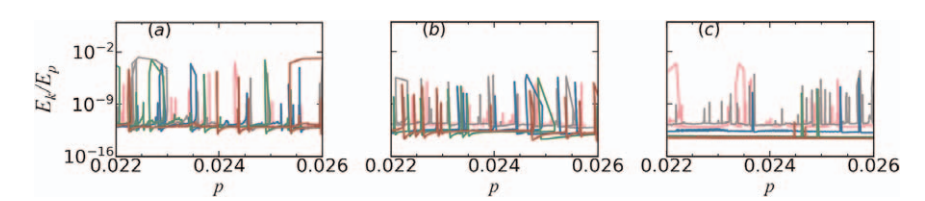


Figure 12.4 Energy ratio E_k/E_p against pressure p for samples prepared with different friction (a) $\mu = 0.0001$, (b) $\mu = 0.1$, and (c) $\mu = 1$; and different tangential stiffness k_t . The different values of k_t/k_n are colored in the following order: 0.001 (red), 0.01 (grey), 0.1 (blue), 0.5 (green), 0.8 (brown).

influenced by the strain rate applied to the system. The results in Figure 12.4 show that the value of k_t plays a role as well. Focusing, for example, on Figure 12.4(b), we note the undershoots are present only for large values of k_t , suggesting that tangential forces play a significant role regarding this part of packing's evolution.

12.3.2.3 Normal (γ_n) and Tangential (γ_t) Viscosity

In DEM simulations, the viscoelastic terms help to accurately represent the dynamic behavior of particles under loading and unloading conditions. Simulations allow for the modeling of phenomena such as stress relaxation, creep, and hysteresis, which are characteristic of granular materials.^{66,67}

The contact model (eqn (12.3) and (12.4)) takes into consideration the energy dissipation and time-dependent behavior of contacting particles *via* viscosity terms along normal (γ_n) and tangential (γ_t) directions. These terms are relevant since the mechanical response of granular assemblies depends not only on the applied load but also on the rate at which the load is applied.

The results that we present next are obtained by using the configurations at $p_z = 0.022$, calculated using the parameters given in Table 12.1, as initial conditions. Starting from these configurations, keeping all inputs as shown in Table 12.1, new simulations are prepared using a few selected values of γ_n and γ_t .

Figure 12.5 shows the results for selected values of γ_n ; since some features of the results are difficult to observe when plotting the whole pressure window [0.022:0.026] that we usually consider, we (also) show additional zoom-ins (parts (d)–(f)) of the figure). We observe that the main effect of γ_n is to modify the decay rate of E_k/E_p , with higher viscosity values leading to a slower decay rate of E_k/E_p ; this effect is most visible in the zoomed-in plots,

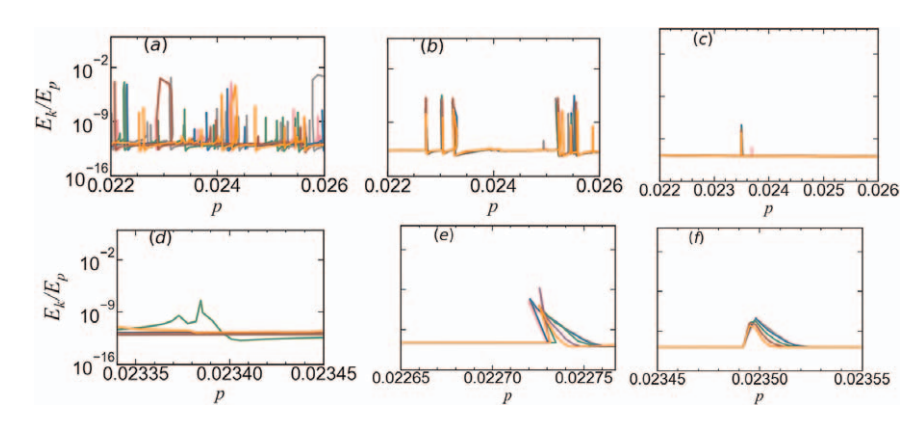


Figure 12.5 Energy ratio E_k/E_p against pressure p for samples prepared with different friction (a) $\mu=0.0001$, (b) $\mu=0.1$, and (c) $\mu=1$; and different tangential viscosity γ_t . The different values of γ_t/γ_n are colored in the following order: 100 (red), 200 (grey), 500 (blue), 2000 (green), 5000 (brown), 10 000 (orange). The parts (d)–(f) are zoom-ins of (a)–(c), respectively.

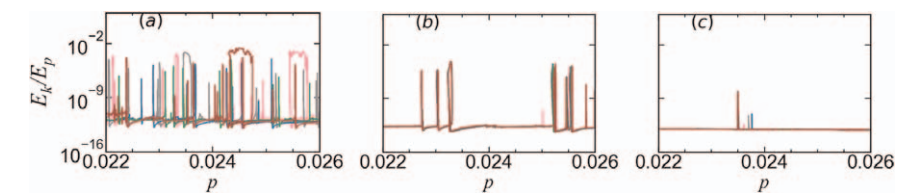


Figure 12.6 Energy ratio E_k/E_p against pressure p for samples prepared with different friction (a) $\mu = 0.0001$, (b) $\mu = 0.1$, and (c) $\mu = 1$; and different tangential viscosity γ_t . The different values of γ_t/γ_n are colored in the following order: 0.01 (red), 0.1 (grey), 0.2 (blue), 1 (green), 2 (brown).

parts (e) and (f) of Figure 12.5. Consistent results are found when γ_t is modified, as shown in Figure 12.6. However, in the case of γ_t , the effect is less pronounced compared to γ_n . The friction coefficient itself does not appear to have any noticeable influence on the decay rate of energy, vis. Figure 12.5(e) and (f).

12.4 Conclusions

In this chapter, we have focused on the compression of granular packings and, in particular, on the insights that can be reached by considering the kinetic energy of the granular particles. The compression process consists of smooth periods interrupted by intermittent "transitions" that correspond to rearrangements of the packings. Therefore, contrary to what might be expected, compression may destabilize a packing, leading to avalanche-like transitions. By considering the influence of various parameters entering the compression protocol, we are able to reach additional insight into the properties of the rearranging transitions.

The transitions are characterized by sudden jumps of the considered kinetic/potential energy ratio, E_k/E_p , followed by the exponential decay. This decay may bring the E_k/E_p ratio either down to the baseline corresponding to smooth compression or even lower, producing undershoots. The magnitude of undershoots and subsequent rise/relaxation to the baseline level are not significantly affected by the value of friction coefficient or viscosity terms. On the contrary, the strain rate $\dot{\varepsilon}$ and tangential stiffness, k_t , are found to have a strong influence on the characteristics of undershoots. Friction itself strongly influences the number of transitions: larger friction coefficients significantly decrease the number of transitions. Furthermore, the base-line of the E_k/E_p ratio is friction dependent: larger friction leads to the lower base-line.

In this chapter, we have primarily focused on the insights obtained by considering the ratio of kinetic to potential energy. However, a deeper understanding can be achieved by considering the statics and dynamics of the contact and interaction networks. Interested readers are encouraged to refer to ref. 19 for a detailed discussion of frictionless results and ref. 20 for the analysis of frictional results. By combining our findings with the comprehensive analysis of frictionless and frictional results in the referenced

works, we have made significant progress in understanding the compression behavior of granular packings. The insights gained from this research contribute to the broader understanding of granular materials and can guide the development of constitutive models for accurately predicting their behavior in various applications.

Acknowledgements

RK and LK acknowledge support from the US Army Research Office Grant No. W911NF1810184; LK also acknowledges support from U. Twente Da Vinci visiting program. KT acknowledges funding from the German Science Foundation (DFG) through the project STE-969/16-1 within the SPP 1897 "Calm, Smooth and Smart".

References

- 1. A. J. Kabla and T. J. Senden, Dilatancy in slow granular flows, *Phys. Rev. Lett.*, 2009, **102**(22), 228301.
- 2. Y. Xiao, L. Long, M. T. Evans, H. Zhou, H. Liu and A. W. Stuedlein, Effect of particle shape on stress-dilatancy responses of medium-dense sands, *J. Geotech. Geoenviron. Eng.*, 2019, 145(2), 04018105.
- 3. B. A. Klumov, Y. Jin and H. A. Makse, Structural properties of dense hard sphere packings, *J. Phys. Chem. B*, 2014, **118**(36), 10761–10766.
- 4. M. Hanifpour, N. Francois, V. Robins, A. Kingston, S. M. Vaez Allaei and M. Saadatfar, Structural and mechanical features of the order-disorder transition in experimental hard-sphere packings, *Phys. Rev. E*, 2015, 91(6), 062202.
- 5. P. A. Cundall and O. D. L. Strack, A discrete numerical model for granular assemblies, *Geotechnique*, 1979, **29**(1), 47–65.
- 6. S. Luding, Introduction to discrete element methods: basic of contact force models and how to perform the micro-macro transition to continuum theory, *Eur. J. Environ. Civ. Eng.*, 2008, **12**(7–8), 785–826.
- 7. D. C. Rapaport, *The Art of Molecular Dynamics Simulation*, Cambridge University Press, 2004.
- 8. K. Taghizadeh, S. Luding, and V. Magnanimo, Dem applied to soil mechanics, in *ALERT Doctoral School 2017 Discrete Element Modeling*, vol. 129, 2017.
- 9. F. Radjai and F. Dubois, *Discrete-element Modeling of Granular Materials*, Wiley-Iste, 2011.
- 10. T. S. Sassel, F. Patino-Ramirez, K. J. Hanley and C. O'Sullivan, Linking the macro-scale response of granular materials during drained cyclic loading to the evolution of micro-structure, contact network and energy components, *Granular Matter*, 2023, 25(2), 23.
- 11. F. Radjai, D. E. Wolf, S. Roux, M. Jean, and J. J. Moreau, Force networks in dense granular media, in *Powders & grains*, 1997, vol. 97, pp. 211–214.

12. C. R. I. Clayton, Stiffness at small strain: research and practice, *Géotechnique*, 2011, **61**(1), 5–37.

- 13. J. P. Bardet, Numerical simulations of the incremental responses of idealized granular materials, *Int. J. Plast.*, 1994, **10**(8), 879–908.
- 14. L. Sibille, F. Nicot, F.-V. Donzé and F. Darve, Analysis of failure occurrence from direct simulations, *Eur. J. Environ. Civ. Eng.*, 2009, **13**(2), 187–201.
- 15. C. S. Chang, S. J. Chao and Y. Chang, Estimates of elastic moduli for granular material with anisotropic random packing structure, *Int. J. Solids Struct.*, 1995, 32(14), 1989–2008.
- 16. S. J. Antony, Link between single-particle properties and macroscopic properties in particulate assemblies: role of structures within structures, *Philos. Trans. R. Soc.*, *A*, 2007, **365**(1861), 2879–2891.
- 17. L. Papadopoulos, J. G. Puckett, K. E. Daniels and D. S. Bassett, Evolution of network architecture in a granular material under compression, *Phys. Rev. E*, 2016, **94**(3), 032908.
- 18. N. P. Kruyt, I. Agnolin, S. Luding and L. Rothenburg, Micromechanical study of elastic moduli of loose granular materials, *J. Mech. Phys. Solids*, 2010, **58**(9), 1286–1301.
- 19. S. Luding, K. Taghizadeh, C. Cheng and L. Kondic, Understanding slow compression and decompression of frictionless soft granular matter by network analysis, *Soft Matter*, 2022, **18**, 1868–1884.
- 20. K. Takhizadeh, S. Luding, R. Basak and L. Kondic, Understanding slow compression of frictional granular particles, *Soft Matter*, 2024, **20**, 6448–6457.
- 21. J. Mei, G. Ma, J. Liu, F. Nicot and W. Zhou, Modeling shear-induced solid-liquid transition of granular materials using persistent homology, *J. Mech. Phys. Solids*, 2023, **176**, 105307.
- 22. S. Ardanza-Trevijano, I. Zuriguel, R. Arévalo and D. Maza, Topological analysis of tapped granular media using persistent homology, *Phys. Rev. E*, 2014, **89**(5), 052212.
- 23. J. W. Landry, G. S. Grest, L. E. Silbert and S. J. Plimpton, Confined granular packings: structure, stress, and forces, *Phys. Rev. E*, 2003, **67**(4), 041303.
- 24. C. Thornton, S. J. Cummins and P. W. Cleary, An investigation of the comparative behaviour of alternative contact force models during inelastic collisions, *Powder Technol.*, 2013, 233, 30–46.
- 25. H. P. Zhang and H. A. Makse, Jamming transition in emulsions and granular materials, *Phys. Rev. E*, 2005, 72(1), 011301.
- 26. K. L. Johnson, Contact Mechanics, Cambridge University Press, 1987.
- 27. C. Thornton, S. J. Cummins and P. W. Cleary, An investigation of the comparative behaviour of alternative contact force models during elastic collisions, *Powder Technol.*, 2011, 210(3), 189–197.
- 28. Y. Li, Y. Xu and C. Thornton, A comparison of discrete element simulations and experiments for 'sandpiles' composed of spherical particles, *Powder Technol.*, 2005, **160**(3), 219–228.

- 29. H. K. Emden, S. Rickelt, S. Wirtz and V. Scherer, A study on the validity of the multi-sphere discrete element method, *Powder Technol.*, 2008, **188**(2), 153–165.
- 30. A. Alenzi, M. Marinack, C. F. Higgs and J. J. McCarthy, Dem validation using an annular shear cell, *Powder Technol.*, 2013, **248**, 131142.
- 31. R. D. Mindlin and H. Deresiewicz, Elastic spheres in contact under varying oblique forces, *J. Appl. Mech.*, 1953, 327–344.
- 32. S. Luding, Cohesive, frictional powders: contact models for tension, *Granular Matter*, 2008, **10**(4), 235–246.
- 33. Y. Tsuji, T. Tanaka and T. Ishida, Lagrangian numerical simulation of plug flow of cohesionless particles in a horizontal pipe, *Powder Technol.*, 1992, 71(3), 239–250.
- 34. K. Giannis, C. Schilde, J. H. Finke, A. Kwade, M. A. Celigueta, K. Taghizadeh and S. Luding, Stress based multi-contact model for discrete-element simulations, *Granular Matter*, 2021, 23(2), 1–14.
- 35. Taghizadeh K., Elasticity and wave propagation in granular materials, PhD thesis, University of Twente, Netherlands, 2019.
- 36. J. Shäfer, S. Dippel and D. E. Wolf, Force schemes in simulations of granular materials, *J. Phys. I*, 1996, **6**(1), 5–20.
- 37. L. E. Silbert, D. Ertas, G. S. Grest, T. C. Halsey and D. Levine, Geometry of frictionless and frictional sphere packings, *Phys. Rev. E*, 2002, **65**(3), 031304.
- 38. S. Luding, So much for the jamming point, *Nat. Phys.*, 2016, **12**(6), 531–532.
- 39. N. Brodu, J. A. Dijksman and R. P. Behringer, Multiple-contact discrete-element model for simulating dense granular media, *Phys. Rev. E*, 2015, 91(3), 032201.
- 40. S. Nezamabadi, T. H. Nguyen, J.-Y. Delenne and F. Radjai, Modeling soft granular materials, *Granular Matter*, 2017, **19**(1), 1–12.
- 41. J. Brujić, S. F. Edwards, D. V. Grinev, I. Hopkinson, D. Brujić and H. A. Makse, 3d bulk measurements of the force distribution in a compressed emulsion system, *Faraday Discuss.*, 2003, **123**, 207–220.
- 42. J. Brujić, P. Wang, C. Song, D. L. Johnson, O. Sindt and H. A. Makse, Granular dynamics in compaction and stress relaxation, *Phys. Rev. Lett.*, 2005, **95**(12), 128001.
- 43. J. Barés, N. Brodu, H. Zheng and J. A. Dijksman, Transparent experiments: releasing data from mechanical tests on three dimensional hydrogel sphere packings, *Granular Matter*, 2020, **22**(1), 17.
- 44. P. Yu, S. Frank-Richter, A. Börngen and M. Sperl, Monitoring three-dimensional packings in microgravity, *Granular matter*, 2014, **16**(2), 165–173.
- 45. E. Alaei, B. Marks and I. Einav, A hydrodynamic-plastic formulation for modelling sand using a minimal set of parameters, *J. Mech. Phys. Solids*, 2021, **151**, 104388.
- 46. F. Da Cruz, S. Emam, M. Prochnow, J.-N. Roux and F. Chevoir, Rheophysics of dense granular materials: Discrete simulation of plane shear flows, *Phys. Rev. E*, 2005, **72**(2), 021309.

47. M. Hassan Khalili, J.-N. Roux, J.-M. Pereira, S. Brisard and M. Bornert, Numerical study of one-dimensional compression of granular materials. i. stress-strain behavior, microstructure, and irreversibility, *Phys. Rev. E*, 2017, **95**(3), 032907.

- 48. R. C. Hurley and J. E. Andrade, Strength of granular materials in transient and steady state rapid shear, *Procedia Eng.*, 2015, **103**, 237245.
- 49. J. Gaume, G. Chambon and M. Naaim, Quasistatic to inertial transition in granular materials and the role of fluctuations, *Phys. Rev. E*, 2011, 84(5), 051304.
- 50. P. Jop, Y. Forterre and O. Pouliquen, A constitutive law for dense granular flows, *Nature*, 2006, 441(7094), 727–730.
- 51. F. Göncü, O. Durán, and S. Luding, Jamming in frictionless packings of spheres: determination of the critical volume fraction, in *AIP Conference Proceedings*, American Institute of Physics, 2009, vol. 1145, pp. 531–534.
- 52. K. Taghizadeh, N. Kumar, V. Magnanimo, and S. Luding, Understanding the effects of inter-particle contact friction on the elastic moduli of granular materials, in *IOP Conference Series: Earth and Environmental Science*, IOP Publishing, 2015, vol. 26, p. 012008.
- 53. M. R. Kuhn and A. Daouadji, Stress fluctuations during monotonic loading of dense three-dimensional granular materials, *Granular Matter*, 2019, 21, 1–14.
- 54. A. Clerc, A. Wautier, S. Bonelli and F. Nicot, Meso-scale signatures of inertial transitions in granular materials, *Granular Matter*, 2021 23(2), 28.
- 55. F. Göncü, O. Durán and S. Luding, Constitutive relations for the isotropic deformation of frictionless packings of polydisperse spheres *C. R. Mec.*, 2010, 338(10–11), 570–586.
- 56. F. Göncü and S. Luding, Effect of particle friction and polydispersity on the macroscopic stress–strain relations of granular materials, *Acta Geotech.*, 2013, **8**, 629–643.
- 57. I. Agnolin and J.-N. Roux, Internal states of model isotropic granular packings. i. assembling process, geometry, and contact networks, *Phys. Rev. E*, 2007, **76**(6), 061302.
- 58. C. S. OHern, L. E. Silbert, A. J. Liu and S. R. Nagel, Jamming at zero temperature and zero applied stress: The epitome of disorder, *Phys. Rev. E*, 2003, **68**(1), 011306.
- 59. N. Kumar and S. Luding, Memory of jamming-multiscale models for soft and granular matter, *Granular Matter*, 2016, **18**(3), 1–21.
- 60. C. Song, P. Wang and H. A. Makse, A phase diagram for jammed matter, *Nature*, 2008, **453**(7195), 629–632.
- 61. J. Brujić, C. Song, P. Wang, C. Briscoe, G. Marty and H. A. Makse, Measuring the coordination number and entropy of a 3d jammed emulsion packing by confocal microscopy, *Phys. Rev. Lett.*, 2007, **98**(24), 248001.
- 62. M. van Hecke, Jamming of soft particles: geometry, mechanics, scaling and isostaticity, *J. Phys.: Condens. Matter*, 2009, 22(3), 033101.

- 63. A. A. Long, D. V. Denisov, P. Schall, T. C. Hufnagel, X. Gu, W. J. Wright and K. A. Dahmen, From critical behavior to catastrophic runaways: comparing sheared granular materials with bulk metallic glasses, *Granular Matter*, 2019, 21(4), 99.
- 64. J. D. Goddard, Nonlinear elasticity and pressure-dependent wave speeds in granular media, *Proc. R. Soc. A*, 1990, **430**(1878), 105–131.
- 65. J. P. Bardet, Observations on the effects of particle rotations on the failure of idealized granular materials, *Mech. Mater.*, 1994, **18**, 159182.
- 66. K. Saitoh, K. Taghizadeh and S. Luding, Sound characteristics of disordered granular disks: effects of contact damping, *Front. Phys.*, 2023, 11, 402.
- 67. B. P. Tighe, Relaxations and rheology near jamming, *Phys. Rev. Lett.*, 2011, **107**(15), 158303.